POLITECNICO DI TORINO
Repository ISTITUZIONALE

Source and defect localization in thin elastic plates of arbitrary geometry using eigenmodes

Original
Source and defect localization in thin elastic plates of arbitrary geometry using eigenmodes / Lott, M., Gliozzi, A.S., Bosia, F.. - In: MECHANICAL SYSTEMS AND SIGNAL PROCESSING. - ISSN 0888-3270. - ELETTRONICO. - 184:(2023), p. 109706. [10.1016/j.ymssp.2022.109706]

Availability:
This version is available at: 11583/2972182 since: 2022-10-11T07:04:55Z

Publisher:
Elsevier

Published
DOI:10.1016/j.ymssp.2022.109706

Terms of use:

This article is made available under terms and conditions as specified in the corresponding bibliographic description in the repository

Publisher copyright
Elsevier postprint/Author's Accepted Manuscript

© 2023. This manuscript version is made available under the CC-BY-NC-ND 4.0 license
http://creativecommons.org/licenses/by-nc-nd/4.0/.The final authenticated version is available online at:
http://dx.doi.org/10.1016/j.ymssp.2022.109706

(Article begins on next page)

27 June 2026

Click here to view linked References

Source and defect localization in thin elastic plates of arbitrary geometry using eigenmodes

Martin Lott, Antonio S. Gliozzi and Federico Bosia*

Department of Applied Science and Technology (DISAT), Politecnico di Torino, Torino, Italy

(Dated: August 17, 2022)

Abstract

In this paper, we experimentally demonstrate how discrete resonances can be used to image acoustic sources and mechanical changes in thin plates with different boundary shapes. The proposed method uses coupled numerical and experimental data processing, and it only requires the knowledge of the sample geometry (and not its elastic properties). If a limited number of measurement points is available in experiments, the free modes of the plates are not orthogonal from the receivers' point of view, and this induces an artificial coupling in the post-processing of the experimental signals. However, we show that this effect can be corrected using numerical simulations and a mathematical transformation of the antenna geometry. After this correction, imaging of active sources is performed using coherent summation of the elastic field over the natural frequencies of the plates, leading to an unique localization of the sources. Imaging mechanical changes in the two plates, instead, is addressed using incoherent summation over the modes, leading to symmetry problems for the plates. This work experimentally illustrates the spatial resolution, perspectives and limitations in the use of eigenmodes to produce images in complex elastic systems of arbitrary shape and materials.

* martin.lott@polito.it

I. INTRODUCTION

Imaging using mechanical waves is a widely used tool not restricted to technological problems. It can be found for example in nature with spiders or bats, which use ultrasounds or elastic waves to scan and image their environment [1, 2]. To be more specific, wave imaging relies on the ability to discern any point in space by recording and processing vibration data. In fluids, if the bulk density ρ and sound celerity c are known, wave diffraction theory can predict in any point and at any time the acoustic wave field inside the medium from measurements at the boundaries [3]. This theory has led to the development of advanced array imaging techniques, used in different fields of research, from wave physics applications [4–7] and medical imaging [8, 9] to seismology [10–12].

In general, a large set of experimental data must be taken into account for the construction of an image. Using matrices to represent and analyze spatiotemporal acoustic data has the advantage of simplifying complex operations like space filtering, beam-forming and wave polarization analysis [13, 14]. In addition, this type of formalism bridges the gap between an analytical formulation and experimental data manipulation, especially with the use of synchronized source/sensor arrays, where the backpropagation operators in space and time can be treated as simple matrix multiplications [3, 15–17]. Usually, diffraction theory for imaging is adopted when the elastic wavelengths are much smaller than the domain to image. In addition, with the use of multi-element arrays, the received waves can be separated based on their arrival direction. This means that the far-field plane waves arriving at the detectors are orthogonal from the receiver array point of view. This limit helps to remove potential unwanted wave reflections and conversions from boundaries, which strongly affect the quality of an image [5].

In the low frequency limit, when the wavelengths are of the same order of magnitude as the domain to be probed, the waves do not propagate and form a so-called standing wave, with discrete resonance effects over frequency. Imaging a medium using its resonant modes is also a wide field of research in itself. Modal Analysis (MA) techniques (also known as System Identification) are used in civil [18], mechanical [19] and aerospace [20] engineering. They are deployed on systems and structures that present complex geometries and boundary conditions, i.e. situations where classical diffraction theory cannot be simply applied [21].

One of the main advantages of MA is that the resonant modes are extended in space.

This means that the entire structure is affected by the vibration, with node and antinode locations that are frequency dependent. Moreover, from an energetic point of view, the lowest frequency modes of a structure gather most of the mechanical energy that the system receives. This restriction in the propagation of energy as a function of frequency for eigenmode may be used to determine the presence of potential defects in a structure, which are very sensitive to the level of vibrational energy[22–27]. However, previous research has shown that among the observable available with MA, the curvature of modal shapes (i.e., the spatial derivative of the modal displacement), and not the resonance frequencies, is the most effective tool for imaging[25, 26, 28], even for a simple one-dimensional structure[21, 26]. This is a strong limitation for the use of modal methods, which consequently require significant instrumentation and mainly surface imaging capabilities.

In the present paper, we propose an experimental realization of modal elastic imaging in an arbitrary elastic system, which draws on both MA and wave diffraction paradigms. The methodology relies on the simultaneous manipulation of multiple discrete modes (eigenmodes), which are present in a highly reverberating system, to image the presence of an active source inside the medium. Similar to the case of traditional elastic imaging methods, one needs to determine the Green's functions for the system to make quantitative comparisons between a model and experimental data. However, in the low frequency regime, there is in general no analytical solution for the Green's function. This is especially true for thin elastic plates with free boundaries, like the one used in the present work. Here, we overcome this limitation with the use of numerical simulations to obtain the eigenfrequencies and eigenmodes of the finite sample. This well-known procedure has yet to be used in this manner for source imaging in elastic systems. The natural frequencies and modal shapes are determined numerically, from a data-driven procedure only requiring knowledge of the sample geometry, enabling to determine the exact elastic properties for the sample under consideration. Subsequently, the numerically calculated modes are combined using a Green's function modal expansion to obtain a semi-analytical propagation model, which can be used to image the system. In addition, from the experimental realization, we highlight the need to exploit the exact receiver positions on the plate surface in the imaging procedure. This requirement is due to the fact that normal modes for the plate are not orthogonal from the receiver point of view, and this leads to post-processing cross-talk between modes and errors

in the image reconstruction. In this paper, we therefore propose and apply a novel and general mathematical method to address this limitation of non-orthogonality. By appropriately combining vibration data and numerical modeling, two imaging problems are addressed: the imaging of an active source and the imaging of a small defect in a reverberating environment. To assess the role of symmetries in the imaging procedures, the experimental setup includes two different thin aluminum plates of different shapes (rectangular and irregular pentagonal). For the source localization problem, a practical situation is chosen where the time emission of the source is unknown, which creates the need to perform another step of phase-locking in the reverberated (coda) part of the transmitted signal. On the other hand, the mass monitoring problem is based on an incoherent summation *in space* over the eigenmodes, which leads to symmetry issues in the resulting images. These symmetry-related errors are driven by the sample geometry only.

The paper is organized as follows. First, we describe the samples and the procedure for acquiring the vibration data. Second, we describe the construction of the digital counterpart of the sample, and the details of the signal processing algorithm. This step holds on synthetic data for illustration purposes of the core of the imaging problem. Third, the experimental source localization images are presented for both samples and compared to the synthetic data. Finally, results and perspectives for defect-like imaging with monitoring techniques using discrete resonant modes are discussed.

II. MATERIALS AND METHODS

A. Experimental set-up

The first sample used in this study is a thin aluminum plate of 3 mm thickness with irregular and non-parallel edges (Fig 1). The particular shape given to the plate guarantees the absence of degenerate modes (i.e. modes with the same resonance frequency but with different modal shapes). Since this study aims to exploit modal imaging concepts, we consider the response at the lowest frequency of the plate. In this frequency regime, the only admitted mode within the plate is the out-of-plane, antisymmetric, dispersive A_0 Lamb mode. For a 3 mm plate, we can determine the wave velocity of this mode from the formula:

$$C_p = \sqrt[4]{\omega^2 \frac{D_0}{h\rho}}; \quad (1)$$

where $D_0 = h^3 E/(12(1-\nu^2))$ is the flexural rigidity, and E, ν, ρ and h are the Young's modulus, Poisson's ratio, bulk density and thickness, respectively. The wavelength is of the order of $\lambda = 50$ cm at 100 Hz, which roughly corresponds to typical plate lateral dimensions (see fig. 1-a), meaning that the 10 lowest modes of this plate should be located around 100 Hz.

The experiment consist in recording at different random locations on the sample the temporal evolution of the wave field generated by various independent active sources. The main purpose of this first experiment is to image the source location, from the analysis of the highly reverberated time signal at the receiver locations. The plate is thus instrumented with 3 piezoelectric disks (ABT-441-RC9, 4.2 kHz central frequency) with a diameter of 27 mm and a thickness of 0.5 mm, which act as the sources. The piezoelectric disks are independently driven with a 2 second chirp signal, with a frequency content ranging from 20 Hz to 900 Hz. This signal is generated by an arbitrary signal generator (Agilent 33500 B), and amplified with an high impedance output tension amplifier (FLC Electonics A400). After propagating in the plate, the vibration response is measured using a Doppler laser vibrometer (Polytech OFV-500 decoder and OFV-505 sensor-head) at 16 different plate locations. The recorded signal is then cross-correlated with the source signal, to provide a 0.5 s highly reverberated impulse response. For each source, the obtained data-set can be represented by a matrix $\mathbf{K_r}(\mathbf{t})$, indexing time at sampling rate intervals and space $r = 1, 2, ..16$ from receiver locations in two dimensions. A schematic of the experiment is shown in Fig. 1-a. Two sources are located on the edges of the plate and one in the center. The receivers are randomly distributed over the plate. A typical example of the 16 recorded signals and their corresponding frequency spectra for a single source are shown in Fig. 1 b-c.

From Fig. 1 panel b-1, one can see that as soon as the signal is emitted, reflected waves appear that mask any potential coherent propagation. From (fig. 1 panel c), the Fourier transforms highlight separated peaks, corresponding to the first resonant modes of the plate.

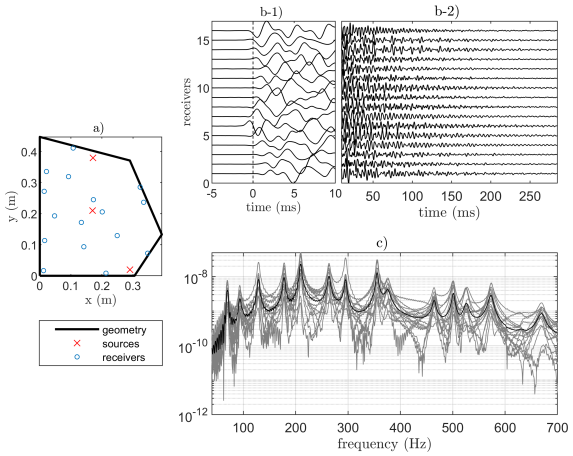

FIG. 1. Irregular plate geometry with its instrumentation. a) For each of the three sources, 16 signals are recorded at the blue location points with a Doppler laser vibrometer, b) with a 300 ms of a strongly reverberated signal (coda). c) In the frequency domain, the signals show clear and isolated resonance peaks. The average of the spectra over the 16 measurement points is represented by the black line.

B. Modal shape determination

The proposed approach exploits knowledge of the modes of vibration to construct a semi-analytical propagating model for the studied sample. There is in the literature a large set of methods able to compute normal modes and associated frequencies for systems with simple geometries [12, 29–31]. Usually, these methods are based on Hamilton's principle of least action, according to which a dynamic system tends to minimize its internal mechanical energy. This minimization principle leads to an eigenvalue problem, with the resonance frequencies as eigenvalues and the normal vibration mode shapes as eigenvector solution of the problem [30]. For the considered plate geometry with Neumann boundary conditions (free edges), analytical models run the risk of non-exhaustively predicting the eigenmodes [19]. A possible solution is to use finite element modeling (FEM) and eigenvalue analysis to obtain the eigenmodes and corresponding eigenfrequencies. The input mechanical parameters (Young's modulus and Poisson's ratio) can then be adjusted to find the best match between the measured and numerically predicted resonance frequencies. This procedure is also know under the name of Resonant Ultrasound Spectroscopy (RUS)[30, 32, 33].

For the source localization procedure to be successful, the numerically calculated and

experimentally derived normal modes should coincide. A way to guarantee this similarity is to perform a systematic spatial projection of numerical modes on the measured ones. This can additionally improve the RUS methodology by simultaneously optimizing the agreement between experimental and numerical data for both the resonant frequencies and modal shapes. To do this, we consider the array response matrix of the three sources s in the frequency domain $\tilde{\mathbf{K}}^{(\mathbf{s})}(\omega)$, projected over the receivers array on the modal shape ϕ_{rn} :

$$B_n(\omega) = \Sigma_s \left| \Sigma_r \tilde{K}_r^{(s)}(\omega)\phi_{rn} \right| \tag{2}$$

$\tilde{\mathbf{K}}^{(\mathbf{s})}(\omega)$ is a matrix, indexed by the *frequencies* and the *receiver index*. This is a table which gathers the measured frequency $\times$ space signals. The product $\tilde{K}_r^{(s)}(\omega)\phi_{rn}$ is therefore a matrix indexed by (*frequency* $\times$ *mode number*).

The starting guess for the mechanical parameter values are $E = 69\ GPa$ for the Young's modulus, $\nu = 0.33$ for the Poisson ration, and $\rho = 2700\ kg.m^{-3}$ for the density , which are the typical aluminum elastic properties. Then, for different Young's modulus and Poisson's ratio values around the starting point, we compute the eigenfrequencies and eigenmodes of the system, and consider the minimization function :

$$g = \Sigma_n \left| \omega_n^d - \omega_n \right| / \omega_n \tag{3}$$

with ω_n^d the angular frequency with the maximum amplitude response of the array projected on the eigenmode ϕ_{rn}, and ω_n the numerical eigenfrequency of this same mode computed from FEM. In this manner, we include the spatial response of the modes in the inversion procedure. Once the minima of g in Eq.3 are found, the results of the projection defined in Eq.2 are depicted in Fig. 2 for optimized mechanical parameters. This figure illustrates the post-processing mode separation over space, with the projection of the experimental data on the numerical eigenmodes. With 16 receivers, the first 13 modes present a maximal projection value $B_n(f = \omega/2\pi)$ at the corresponding eigenfrequency $f_n = \omega_n/2\pi$. Final values are $E = 69.6\ GPa$ for the Young's modulus and $\nu = 0.345$ for the Poisson ratio. Note that an error in the determination of the geometry of the sample could be translated in an uncertainty in the estimated mechanical parameters.

The normalized vibration profiles of the first 16 eigenmodes are shown in Fig 3. The sharp corners used for the design of the plate create a clear separation between modes. From the

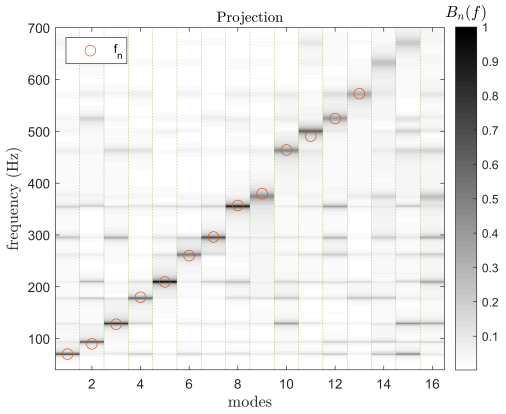

FIG. 2. Frequency response of the normalized modal projection. The red circle represents the eigenfrequency values computed with FEM. The gray-scale represents the continuous response over frequency for each mode, projected (eq.2) on the FEM eigenmodes.

modal fields, the maximum displacement zones appear to be located at the edges of the plate, whilst the nodes of vibrations are principally located in the center of the sample.

C. Modal Green's function expansion and source localization principle

The spatiotemporal evolution of the wave field inside the plate is derived using a universal Green's function expansion method, which only requires knowledge of the normal modal shapes and the associated eigenfrequencies. We start from the expression of the Green's function in the time domain (for $t > 0$)[34–37]:

$$G_{ij}(t) = \Sigma_n \phi_{in} \phi^{\dagger}_{nj} \cos(\omega_n t) \tag{4}$$

where i, j denote the location of two points in the continuous sample domain Ω, n designates the modal index, ω_n the angular eigenfrequency and ϕ_{in} the n-th eigenmode amplitude at the point i. The symbol $.^{\dagger}$ designates the transpose conjugate, and ϕ_{in} are the standing modes, thus represented by real functions. However, Eq.4 is valid for complex function shape too, as soon as they satisfy the wave equation. The time Fourier transform of the Green's function, computed from $t = 0$ to infinity can be expressed as follows :

$$\tilde{G_{ij}}(\omega) = \Sigma_n \phi_{in} \phi^{\dagger}_{nj} \times \delta(\omega - \omega_n) \tag{5}$$

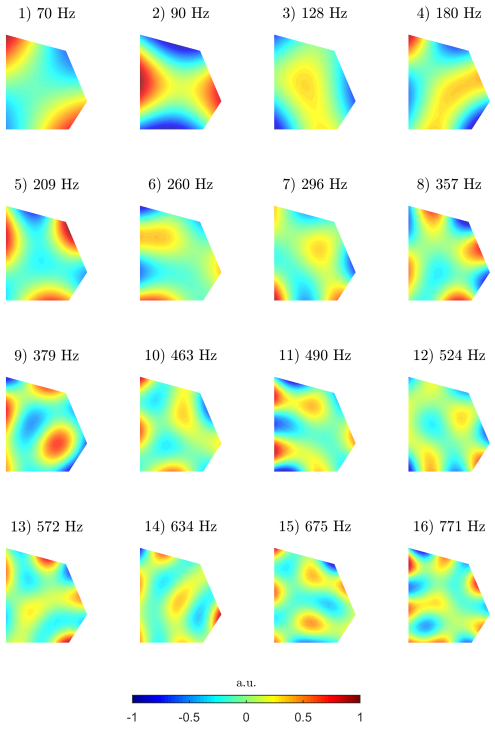

FIG. 3. The 16 first modal shapes of the aluminum plate obtained with FEM.

where $\delta(\omega - \omega_n)$ is the continuous delta function. From this expression, we can express the broadband Green's function, with a continuous integration over frequency:

$$G_{ij} = \int_0^\infty \tilde{G_{ij}}(\omega)\mathrm{d}\omega = \phi_{in}\phi_{nj}^\dagger \tag{6}$$

where we have used Einstein's convention for summation over repeated indices. The upper limit of the continuous sum is determined by the number of modes considered in the imaging problem. With current notations, one should verify:

$$\begin{aligned} \phi_{in}\phi_{nj}^\dagger &= \delta_{ij} \\ \phi_{ni}^\dagger\phi_{in'} &= \delta_{nn'} \end{aligned} \tag{7}$$

where δ_{ij} is the discrete delta function. The first equation indicates that the finite sample response to a source is unique and only depends on its geometrical location. The second equation illustrates the spatial orthogonality of the modal shape functions. To separate the experimental data from theoretical data, the quantity G_{ir} denotes the data set $\mathbf{K_r}(\omega)$, which

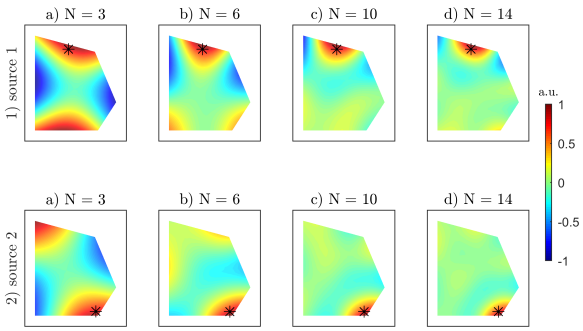

FIG. 4. Synthetic source reconstruction for two different location (1-2) and using 3, 6, 10 and 14 modes respectively.

is the Green's function over frequency, between a source located in an unknown position "i", and a set of receivers located in "r". Because for an arbitrary set of receiving points "r", equations 7 are not satisfied, we present in the following a general method to integrate the geometry of the receiver array. The imaging process then translates the receiving matrix $\mathbf{K_r}(\omega)$ to a single, and frequency accumulated image of the source on the plate surface.

Using these concepts, and the modal responses shown in Fig. 3, we first evaluate the effect of the number of modes on the source reconstruction. From equation 6, the source image is obtained by multiplying the modal amplitude vector at the source location ϕ_{in}, with the modal response matrix at any point location of the sample (and not only the "r" receivers' points) $\phi^{\dagger}_{nj}$. Results are shown in Fig. 4. As expected, increasing the number of modes increases the resolution of the source reconstruction. In addition, the location of the sources also affects the sharpness of the focus.

The central problem of imaging the source lies in the fact that from an experimental point of view, equation 7 is not satisfied when using a small subset of measurement points in the continuous Ω domain. However, it is still possible to construct an image of the source using the composition of Green's function within a set of virtual sources and receiver points r:

$$
\begin{aligned}
G_{ij} &= G_{ir} G_{rj} \\
&= \phi_{in} \phi^{\dagger}_{nr} \phi_{rn'} \phi^{\dagger}_{n'j} \\
&= \phi_{in} V_{nn'} \phi^{\dagger}_{n'j}
\end{aligned} \tag{8}
$$

The matrix $\mathbf{V}$ quantifies the ability of any subsequent set of points r inside the Ω domain to independently identify each mode. If the implicit summation over r is performed on the full domain Ω, the Green's function composition is indeed equivalent to equation 6, and we must verify that:

$$
V_{nn'} = \delta_{nn'} \tag{9}
$$

The projection error due to the limited number of receivers can be corrected. Indeed, with a finite number of modes and receivers, we can determine a new ψ_m basis, constructed as linear combination of the modal shapes ϕ_n. This new basis must be orthonormal from the point of view of the receivers. The construction operation corresponds to the qr-decomposition, which establishes that any rectangular matrix can be decomposed into the product of an orthogonal matrix $\mathbf{Q}$ and an upper triangular matrix $\mathbf{R}$:

$$
\phi^{\dagger}_{nr} = Q_{nm} R_{mr} \tag{10}
$$

where $\mathbf{R}$ matches the receivers to the new basis $\{\psi_m\}$, constructed as linear combination of the modal basis $\{\phi_n\}$. $\mathbf{Q}$ matches the new basis $\{\psi_m\}$ to the modal basis $\{\phi_n\}$. If $\mathbf{R}$ is invertible, the qr-decomposition is unique.

The expression of the Green's function G_{ir} in the new frame basis is noted $G'_{i\{\psi_m\}}$ and can be expressed as:

$$
G'_{i\{\psi_m\}} = G_{ir} R^{-1}_{rm} \tag{11}
$$

Using the correspondence between the $\{\phi_n\}$ and $\{\psi_m\}$ basis, and back-projecting the wave field into each pixel of the image, we can write a potential Green function $\tilde{G_{ij}}$ as:

$$
\tilde{G_{ij}} = G_{ir} R^{-1}_{rm} Q^{\dagger}_{mn'} \phi_{n'j} \tag{12}
$$

We can prove that this expression is the Green's function reconstruction, from the source i to each pixel j, using only r points in the domain Ω. It is valid if the inverse of the matrix $\mathbf{R}$ exists. This means that $\mathbf{R}$ needs to be (but this is not a sufficient condition) a square matrix (i.e. same number of receivers and modes) :

$$\tilde{G_{ij}} = G_{ir} R^{-1}_{rm} Q^{\dagger}_{mn'} \phi^{\dagger}_{n'j} = \phi_{in} \phi^{\dagger}_{nj} = G_{ij} \tag{13}$$

Thus, the imaging principle relies here on the inversion of the matrix $\mathbf{R}$. G_{ir} is a measured quantity, meaning the signal originating from a source and recorded at the receiver locations r, and $\mathbf{Q}$ and $\boldsymbol{\phi}$ are obtained from the QR-decomposition and the FEM model. It is possible to validate the approach with synthetic signals. Here, we limit the example to a single source location, detected with 14 receivers, randomly located over the sample, as shown on fig. 5-a. We first compute the direct, non-corrected, Green's function composition that we applied to the 14 laser measurement point array, following eq. 8. Results are shown in fig.5 b-1 for the matrix $V_{nn'}$ and b-2 for the reconstructed field. The presence of non-zero values on the off-diagonal elements of the $V_{nn'}$ matrix in fig.5 b-1 quantifies the cross-talk between the normal modes due to the limited number of receivers. This leads to spatial errors in the source imaging process. On the other hand, if we apply the qr-decomposition and backproject it using the modified basis (Eq. 12), cross-talk between modes is eliminated and source reconstruction is considerably improved (Fig. 5 c-1 and c-2). Here, signal reconstruction is performed using only a number of receivers equal to the number of modes ($N = 14$).

III. RESULTS

A. Phase locking

Application of the proposed method to real data requires incorporating the effect of time into the modeling. This step is necessary to make a quantitative transition from the measured matrix $\mathbf{K_r}(t)$ and the broadband source model G_{ij}. At time $t = 0$, when the initial pulse is transmitted by the piezoelectric disks, each frequency making up the signal, as a starting point, acquires the phase of the modal shapes at the source location. For stationary modes, this original phase is equal to 0 or π. If this phase information is lost, i.e. we no longer know when the pulse was emitted, the resulting sum in equation 6 leads to an

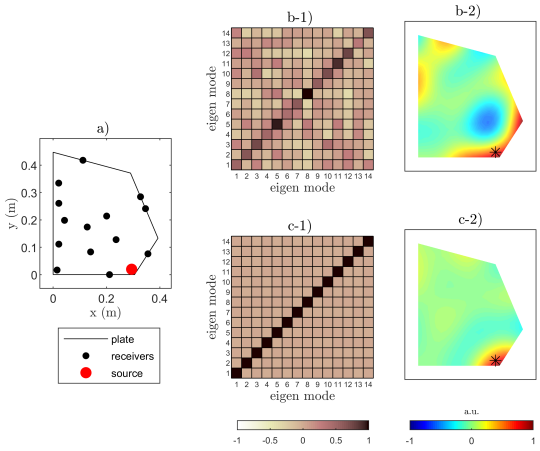

FIG. 5. Principle of source reconstruction with synthetic data. a) Specimen geometry with virtual receivers and source location. b) Using direct Green's function composition leads to a distortion of the matrix $V_{nn'}$ (Eq. 9) (b-1) and errors in the reconstructed signal (b-2). c) Using the array correction, each virtual mode is independent (c-1) and returns an exact image of the source, for the considered modes combination (c-2).

incoherent summation of the modes and to the loss of spatial resolution. A general method for the inversion of the time origin of an active source is presented in [16]. We propose here a simpler solution to this problem, exploiting the fact that the space-time Fourier transform of the receiver array is real, according to Eq. 5.

$\mathbf{K_r(t)}$ is the matrix of receiver data, which records the temporal coda (reverb) signal from a single source in the plate, transmitted at time $t = 0s$ but recorded starting at an unknown time $t_0 > 0s$. For each resonant mode, we consider the delayed-time Fourier transform of the spatial projection, computed from time $t = t_0$ over a time window T:

$$\tilde{F}_n(\omega, t_0 - \tau) = \exp\left(i\omega(t_0 - \tau)\right) \int_0^T K_r(t)\phi_{rn} \exp\left(i\omega t\right) \mathrm{dt} \tag{14}$$

Since $\tilde{F}_n(\omega, t_0 - \tau)$ should be real for all n, we look for the minimum of the function:

$$h_{t_0}(\tau) = \frac{1}{N}\Sigma_n \frac{\left|\Im\left\{\tilde{F}_n(\omega_n, t_0 - \tau)\right\}\right|}{\left|\tilde{F}_n(\omega_n, t_0 - \tau)\right|} \tag{15}$$

where $\Im$ indicates the imaginary part operator. This procedure is graphically illustrated in Fig. 6. In panel a), the signal emitted from source 2 to receiver 5 is shown. From this signal, we apply a Hanning time window in the late part of the coda, starting at $t_0 = 20$ ms, shown in panel b). For eight of the modes with the best signal to noise ratio, the function $\tilde{F}_n(\omega, t_0 - \tau)$ is computed and depicted in panel c). For $\tau = 20$ ms, all modes are synchronized, which corresponds to the delay $\tau = t_0$. The sum over the modes $h_{t_0}(\tau)$ is presented in sub panel c). Thus, even if t_0 (i.e. the temporal origin of the signal) is unknown, it is possible to trace back the origin of the signal using the spatiotemporal analysis of the coda. This is used as a "phase locking" method on the data through the $\tilde{F}_n$ function. Once τ is found, the Green function is estimated as the coherent sum of the delayed Fourier transform of the receiver matrix $\mathbf{K}_r(t)$:

$$G_{ir} = \int_0^\infty \tilde{\mathbf{K}}_r(\omega) \exp\left(-i\omega\tau\right) \mathrm{d}\omega \tag{16}$$

With i the source location (unknown) and r the receiver locations. Rather than using short and impulsive source signals, we use here the stability of the Fourier transform computed over a large window to measure each of the modal amplitudes. This measurement stability may be disrupted when noise becomes prominent in the reverberated signal. From our experimental data, we can analyze the first 200 ms of reverberated signal only, before the measurement is dominated by uncorrelated noise.

B. Experimental source localization

In order to experimentally determine the source location in the considered plate, the real part of the Fourier transform after the phase correction is summed over the eigenfrequencies according to Eq.6 and the resulting vector is back-propagated according to Eq. 12. The theoretical reconstruction model for three examples of source location on the considered plate is displayed Fig. 7-a, experimental results are shown in Fig. 7-b, and the reconstruction without correction in Fig. 7-c. The images in Fig. 7-b show that the reconstruction is effective in determining the location close to the expected theoretical image (Fig.7-a), although the resolution is in some cases limited. In Fig.7, we only use a reduced number of modes with the highest signal to noise ratio in the reconstruction and adapt the array size to keep the possibility to compute the inverse matrix $\mathbf{R}^{-1}$ in equation 12. The reduction of

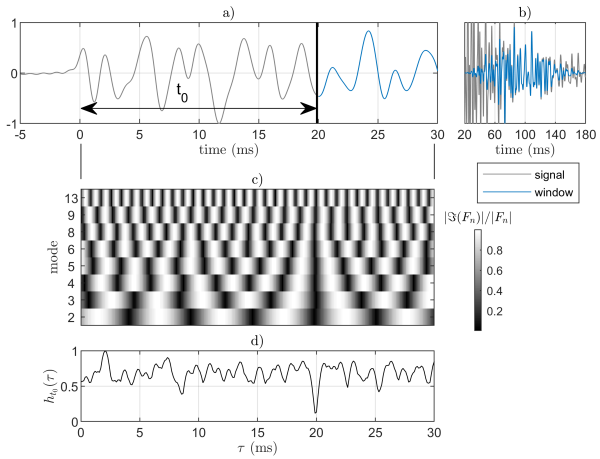

FIG. 6. Phase locking method. a) Time signal emitted from source 2 and recorded at location 5. The considered time window for the analysis starts at time $t_0 = 20\ ms$, highlighted with the black vertical line. b) Hanning time window considered for the analysis (blue signal) of length $T = 160\ ms$ in the late coda part of the total transmitted signal (gray signal). c) Imaginary part contribution of the Fourier transform for 8 modes with the highest signal to noise ratio. d) At $\tau = t_0 = 20\ ms$, all the modes are in sync, which corresponds to a minimum for the function $h_{t_0}(\tau)$

the number of useful modes is due to the imperfection of the source, which does not provide a perfectly flat response in the considered frequency range. In addition, if the source is located on a vibration node of the plate, this mode cannot be excited. These are limiting factors in the efficiency of the method. In the present work, we use the modal amplitude directly estimated in the late coda part of the signal, without further post-processing and we only consider modes with the highest signal to noise ratio. A more accurate approach would need to invert location and modal normalization at the same time.

C. Application to regular geometry

To evaluate the influence of specimen geometry, we produce the same data-set as previously on a 3 mm thick rectangular aluminum plate. Both plates have the same thickness and approximately the same lateral dimensions. For the determination of the modal shapes, we adopt here a semi-analytical method, the xyz algorithm [30]. The resulting first 16 eigenmodes and eigenfrequencies calculated using this method are shown in Fig. 8.

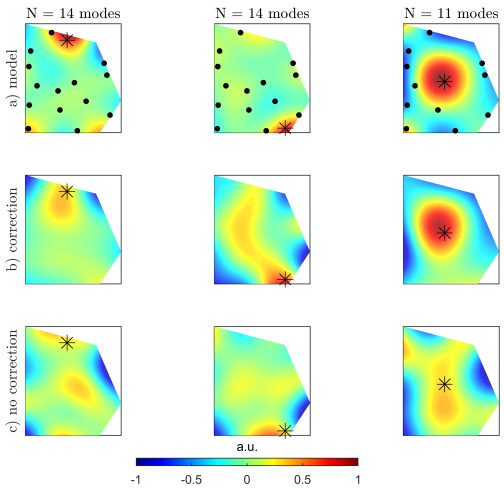

FIG. 7. Images of the reconstruction. panels a) show the expected image with the used receivers as black points and the source as a black star. b) the main resulting image after corrections. Panels c) show the results without correction, for comparison purpose. The images are normalized by the maximum of their absolute value.

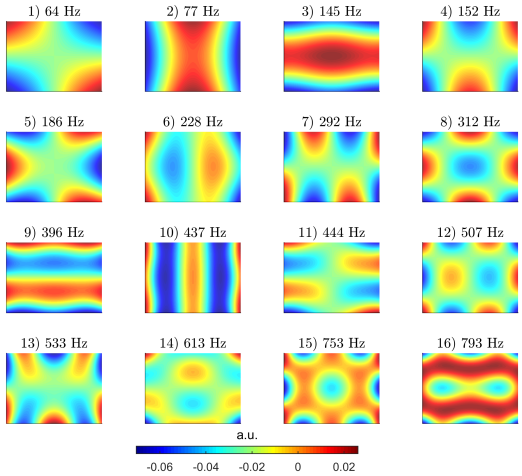

FIG. 8. The 16 first modal shape of the rectangular aluminum plate

Fig. 9 illustrates graphically the results of source localization in three examples for this plate geometry. There is good agreement between the model and the data. In this experiment, only 9 modes are correctly detected and therefore used in the source reconstruction. The number of points used is also reduced to 9, in order to use equation 12.

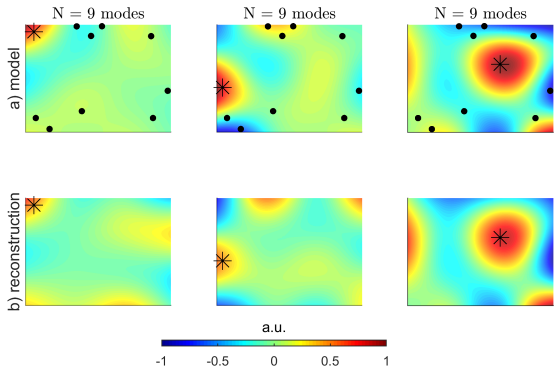

FIG. 9. Sources localization results in the rectangular plate. a) expected image, built from direct Green's function modal expansion. The black dots represents the used receivers for the imaging, and the title specify the number of modes used for the reconstruction. b) reconstruction with the data. The images are normalized by the maximum of their absolute value.

IV. DEFECT LOCALIZATION

The second experiment presented in this work illustrates the feasibility of using the modal imaging method for the detection of inhomogeneities in the tested samples. This is realized by placing a small point mass on the surface of the plates and acquiring the same data set as previously (3 sources, 16 receiver points). The test is performed with both the rectangular and the irregularly shaped plates. Experimentally, a simple perturbation of the dynamic response of the plate is obtained by adding a small mass at its surface. The added mass consists of small cubic permanent magnets. The estimated added mass is around 5g for both plates, which is large enough to be detected but small enough not to change the system overall response. It is possible to use perturbation theories to model this small change in the structure [20, 38]. As a first approximation, we assume here that a change of mass does not affect the eigenmodes shapes $\{\phi_n\}$ but only the eigenfrequencies f_n [27]. This assumption leads to considerable simplifications by neglecting the details of the mechanical interaction of the mass with the plate. Consequently, the mass location can be deduced from the sensitivity of the modes to its addition [39].

We first compare the data set obtained on the pentagonal plate with and without the added mass. The signature of the added mass on the signals is shown in Fig. 10. From the frequency analysis of the data (Fig.10 a-b), the addition of mass induces a shift of the

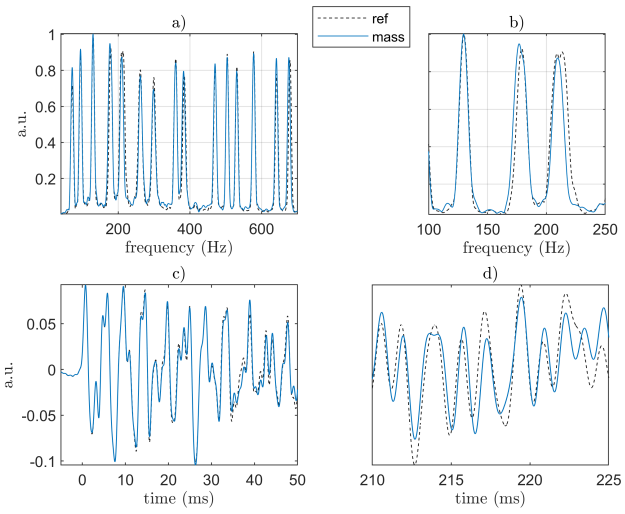

FIG. 10. Signal signatures due to the addition of localized mass. a) The amplitudes and the resonant frequencies are affected by the add of mass. b) (zoom in panel a) The mass decreases the initial resonant frequencies. c) In the time domain, the shift of the resonances are translated into a cumulative phase shift in the coda signal. d) same as c) with a zoom in the 30-60 ms time window.

resonant curves to lower frequencies and a modulation of the peak amplitudes. In the time domain (Fig.10 c-d), we observe the typical cumulative time shift of the coda [40], induced here by the changes of the resonant frequencies. From this complex signature, we choose to retain only the frequency shift of the modes as the main localization parameter and propose the following simplified imaging function :

$$I_i = \Sigma_n \frac{\delta f_n}{f_n} \left|\phi^{\dagger}_{ni}\right| \tag{17}$$

Where i indicates the pixel of the image to be constructed, f_n the n^{th} resonance frequency for the unperturbed plate, and δf_n the variation of a resonance frequency between the reference and perturbed states.

Results of this imaging procedure are shown in Fig. 11 for both rectangular (a) and irregular (b) plates. Since perturbation theory is applied on a mode at a time, it is not possible to perform coherent summations over frequencies as in the previous source localization problem. Thus, localizing a change in a structure from the analysis of individual resonances results in symmetry problems during the data post-processing. For a rectangular shaped structure, the incoherent summation over the modes of the wavefield shown in

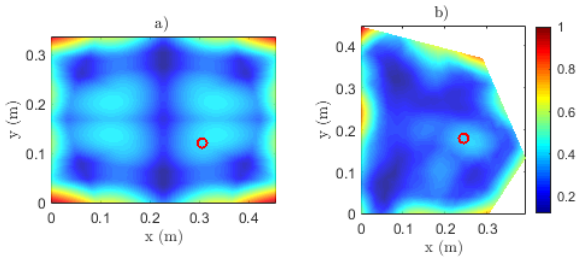

FIG. 11. Mass localization results for a) the rectangular plate with an add mass of 7.2g and b) for the pentagonal plate with an add of mass of 3.6g. the mass is a small magnet depicted with the red circle in panels a-b. The images are normalized by the maximum of their absolute value.

equation 17 leads to four symmetric source images. The irregular pentagonal plate, instead, demonstrates greater uniqueness in the potential location of the mass.

In Fig. 11, the edges of the plates show the largest incoherent cumulative amplitudes of vibration. The use of sharp corners for the two plates helps to split the different resonant modes across frequencies, but also induces nonuniform localization of the vibration energy for the resonant modes. Plates with smooth edges provides a more uniform spatial spread of the energy, and thus modal overlapping over frequency [41, 42], which may add complexity to the modal decomposition technique. The resulting image, built from equation 17, does not take into account the spatial inhomogeneity of the coherent sum over the modes. This is also a factor preventing access to the mass of the added object, as it should be inverted jointly with its location.

V. CONCLUSIONS

In this paper, we have presented the experimental realization of a source and defect-like elastic imaging procedure, using discrete normal modes of plates with arbitrary geometries. The imaging methodologies are based on data-driven procedures, which couple numerical simulations with experimental data.

The first experiment, i.e. source localization, uses a modal Green's function expansion and composition. Sources are shown to be reliably imaged using a coherent sum over the discrete resonant modes supported by the plates, with a mathematical correction for the

receiver array geometry. With the limited number of modes and receivers used in both plates, the resolution of the images are limited but could be applied to any kind of geometry.

The second imaging problem, i.e. mass localization, is handled with an incoherent summation over the same modes, and can lead to symmetry problems due to the plate geometries in the formation of the final images. The incoherent summation of the modes induces four symmetric mass images in the rectangular cavity, and a single one in the irregular pentagonal cavity. For both cavities, the modal intensity is not homogeneous and creates an over-representation of the plate edges in the images.

If the vibration amplitude is large enough, the interaction of the mass with the plate can generate harmonics in a nonlinear regime. These harmonics can be used for imaging, by treating the defect as an auxiliary source. However, the defect must have an impedance comparable to the plate to be treated as an auxiliary source of nonlinear harmonics in the low frequency regime. Another important aspect it that the plate is an anharmonic cavity, meaning that normal modes are not necessarily multiples of fundamental frequencies. The harmonics due to the presence of a defect can alternatively be evanescent, remaining in the defect area, or strongly amplified, if one of the generated harmonics falls on a fundamental mode of the plate. In future, the coherent source imaging technique could be used in reversed mode, using few sources and adapting an array geometry to focus a high level of energy anywhere inside a medium, even at depth, without the need to physically access the targeted point. We will address this method in future work.

ACKNOWLEDGMENTS

We wish to thank Andrea Colombi for valuable discussions and suggestions. All authors are supported by the European Commission under the FET Open "Boheme" Grant No. 863179.

REFERENCES

[1] F Bosia, V Dal Poggetto, AS Gliozzi, G Greco, M Lott, M Miniaci, F Ongaro, M Onorato, SF Seyyedizadeh, M Tortello, et al. Optimized structures for vibration attenuation and sound control in nature: a review. arXiv preprint arXiv:2201.05795, 2022.

[2] Vinícius F Dal Poggetto, Federico Bosia, Gabriele Greco, and Nicola M Pugno. Prey impact localization enabled by material and structural interaction in spider orb webs. Advanced Theory and Simulations, page 2100282, 2021.

[3] Arthur B Baggeroer, WA Kuperman, and Henrik Schmidt. Matched field processing: Source localization in correlated noise as an optimum parameter estimation problem. The Journal of the Acoustical Society of America, 83(2):571–587, 1988.

[4] Claire Prada, Sébastien Manneville, Dimitri Spoliansky, and Mathias Fink. Decomposition of the time reversal operator: Detection and selective focusing on two scatterers. The Journal of the Acoustical Society of America, 99(4):2067–2076, 1996.

[5] Alexandre Aubry and Arnaud Derode. Detection and imaging in a random medium: A matrix method to overcome multiple scattering and aberration. Journal of Applied Physics, 106(4):044903, 2009.

[6] Alexandre Aubry, Laura A Cobus, Sergey E Skipetrov, Bart A Van Tiggelen, Arnaud Derode, and John H Page. Recurrent scattering and memory effect at the anderson localization transition. Physical review letters, 112(4):043903, 2014.

[7] Eric Larose, Thomas Planes, Vincent Rossetto, and Ludovic Margerin. Locating a small change in a multiple scattering environment. Applied Physics Letters, 96(20):204101, 2010.

[8] Jean-Luc Robert and Mathias Fink. Green's function estimation in speckle using the decomposition of the time reversal operator: Application to aberration correction in medical imaging. The Journal of the Acoustical Society of America, 123(2):866–877, 2008.

[9] Massimiliano Fasi, Nicholas J Higham, and Bruno Iannazzo. An algorithm for the matrix lambert w function. SIAM Journal on Matrix Analysis and Applications, 36(2):669–685, 2015.

[10] Andrea Colombi, Julien Chaput, Florent Brenguier, Gregor Hillers, Philippe Roux, and Michel Campillo. On the temporal stability of the coda of ambient noise correlations. Comptes Rendus Geoscience, 346(11-12):307–316, 2014.

[11] Rita Touma, Thibaud Blondel, Arnaud Derode, Michel Campillo, and Alexandre Aubry. A distortion matrix framework for high-resolution passive seismic 3-d imaging: application to the san jacinto fault zone, california. Geophysical Journal International, 226(2):780–794, 2021.

[12] Piero Poli, Michel Campillo, and Maarten de Hoop. Analysis of intermediate period correlations of coda from deep earthquakes. Earth and Planetary Science Letters, 477:147–155, 2017.

[13] Valerio Poggi and Donat Fäh. Estimating rayleigh wave particle motion from three-component array analysis of ambient vibrations. Geophysical Journal International, 180(1):251–267, 2010.

[14] Léonard Seydoux, Julien de Rosny, and Nikolai M Shapiro. Pre-processing ambient noise cross-correlations with equalizing the covariance matrix eigenspectrum. Geophysical Journal International, 210(3):1432–1449, 2017.

[15] William Lambert, Laura A Cobus, Thomas Frappart, Mathias Fink, and Alexandre Aubry. Distortion matrix approach for ultrasound imaging of random scattering media. Proceedings of the National Academy of Sciences, 117(26):14645–14656, 2020.

[16] Michael D Collins and WA Kuperman. Focalization: Environmental focusing and source localization. The Journal of the Acoustical Society of America, 90(3):1410–1422, 1991.

[17] Mathias Fink, Didier Cassereau, Arnaud Derode, Claire Prada, Philippe Roux, Mickael Tanter, Jean-Louis Thomas, and François Wu. Time-reversed acoustics. Reports on progress in Physics, 63(12):1933, 2000.

[18] Ariana Lucia Astorga, Philippe Gueguen, Jacques Riviere, Toshihide Kashima, and Paul Allan Johnson. Recovery of the resonance frequency of buildings following strong seismic deformation as a proxy for structural health. Structural Health Monitoring, 18(5-6):1966–1981, 2019.

[19] Ivo Senjanović, Marko Tomić, Nikola Vladimir, and Neven Hadžić. An analytical solution to free rectangular plate natural vibrations by beam modes–ordinary and missing plate modes. Transactions of FAMENA, 40(3):1–18, 2016.

[20] A Agneni, L Balis Crema, A Castellani, and F Mastroddi. Damage detection on aeronautical structures by a mixed approach in the frequency domain. volume 2768, page 1415, 1996.

[21] Philippe Roux, Philippe Guéguen, Laurent Baillet, and Alaa Hamze. Structural-change localization and monitoring through a perturbation-based inverse problem. The Journal of the Acoustical Society of America, 136(5):2586–2597, 2014.

[22] Peter Cawley and Robert Darius Adams. The location of defects in structures from measurements of natural frequencies. The Journal of Strain Analysis for Engineering Design, 14(2):49–57, 1979.

[23] Charles R Farrar and David A Jauregui. Comparative study of damage identification algorithms applied to a bridge: I. experiment. Smart materials and structures, 7(5):704, 1998.

[24] Jag Humar, Ashutosh Bagchi, and Hongpo Xu. Performance of vibration-based techniques for the identification of structural damage. Structural Health Monitoring, 5(3):215–241, 2006.

[25] Jesús N Eiras, Cédric Payan, Sandrine Rakotonarivo, and Vincent Garnier. Damage detection and localization from linear and nonlinear global vibration features in concrete slabs subjected to localized thermal damage. Structural Health Monitoring, 20(2):567–579, 2021.

[26] Koen Van Den Abeele. Multi-mode nonlinear resonance ultrasound spectroscopy for defect imaging: An analytical approach for the one-dimensional case. The Journal of the Acoustical Society of America, 122(1):73–90, 2007.

[27] Martin Lott, Cedric Payan, Vincent Garnier, Pierre-Yves Le Bas, Timothy James Ulrich, and Marcel C Remillieux. Three-dimensional modeling and numerical predictions of multimodal nonlinear behavior in damaged concrete blocks. The Journal of the Acoustical Society of America, 144(3):1154–1159, 2018.

[28] AS Gliozzi, M Nobili, and M Scalerandi. Modelling localized nonlinear damage and analysis of its influence on resonance frequencies. Journal of Physics D: Applied Physics, 39(17):3895, 2006.

[29] Yongliang Wang, Xinwei Wang, and Yong Zhou. Static and free vibration analyses of rectangular plates by the new version of the differential quadrature element method. International Journal for Numerical Methods in Engineering, 59(9):1207–1226, 2004.

[30] A_ Migliori, JL Sarrao, William M Visscher, TM Bell, Ming Lei, Z Fisk, and R Gi Leisure. Resonant ultrasound spectroscopic techniques for measurement of the elastic moduli of solids. Physica B: Condensed Matter, 183(1-2):1–24, 1993.

[31] T Mizusawa. Natural frequencies of rectangular plates with free edges. Journal of Sound and Vibration, 105(3):451–459, 1986.

[32] Brian J Zadler, Jérôme HL Le Rousseau, John A Scales, and Martin L Smith. Resonant ultrasound spectroscopy: theory and application. Geophysical Journal International, 156(1):154–169, 2004.

[33] Marcel C Remillieux, TJ Ulrich, Cédric Payan, Jacques Rivière, Colton R Lake, and Pierre-Yves Le Bas. Resonant ultrasound spectroscopy for materials with high damping and samples of arbitrary geometry. Journal of Geophysical Research: Solid Earth, 120(7):4898–4916, 2015.

[34] Richard L Weaver and John Burkhardt. Weak anderson localization and enhanced backscatter in reverberation rooms and quantum dots. The Journal of the Acoustical Society of America, 96(5):3186–3190, 1994.

[35] Thomas Gallot, Stefan Catheline, and Philippe Roux. Coherent backscattering enhancement in cavities. highlights of the role of symmetry. The Journal of the Acoustical Society of America, 129(4):1963–1971, 2011.

[36] Stefan Catheline, Thomas Gallot, Philippe Roux, Guillemette Ribay, and Julien De Rosny. Coherent backscattering enhancement in cavities: The simple-shape cavity revisited. Wave motion, 48(3):214–222, 2011.

[37] Philippe Guéguen, Pierre-Yves Bard, and Francisco J Chávez-García. Site-city seismic interaction in mexico city–like environments: An analytical study. Bulletin of the seismological society of America, 92(2):794–811, 2002.

[38] LY Yam, TP Leung, DB Li, and KZ Xue. Theoretical and experimental study of modal strain analysis. Journal of Sound and vibration, 191(2):251–260, 1996.

[39] Zhi-Fang Fu and Jimin He. Elsevier, 2001.

[40] Roel Snieder, Alexandre Grêt, Huub Douma, and John Scales. Coda wave interferometry for estimating nonlinear behavior in seismic velocity. Science, 295(5563):2253–2255, 2002.

[41] Andrea Colombi, Lapo Boschi, Philippe Roux, and Michel Campillo. Green's function retrieval through cross-correlations in a two-dimensional complex reverberating medium. The Journal of the Acoustical Society of America, 135(3):1034–1043, 2014.

[42] Martin Lott, Philippe Roux, Léonard Seydoux, Benoit Tallon, Adrien Pelat, Sergey Skipetrov, and Andrea Colombi. Localized modes on a metasurface through multiwave interactions. Physical Review Materials, 4(6):065203, 2020.

Source and defect localization in thin elastic plates of arbitrary geometry using eigenmodes

Martin Lott, Antonio S. Gliozzi and Federico Bosia*

Department of Applied Science and Technology (DISAT), Politecnico di Torino, Torino, Italy

(Dated: August 17, 2022)

Abstract

In this paper, we experimentally demonstrate how discrete resonances can be used to image acoustic sources and mechanical changes in thin plates with different boundary shapes. The proposed method uses coupled numerical and experimental data processing, and it only requires the knowledge of the sample geometry (and not its elastic properties). If a limited number of measurement points is available in experiments, the free modes of the plates are not orthogonal from the receivers' point of view, and this induces an artificial coupling in the post-processing of the experimental signals. However, we show that this effect can be corrected using numerical simulations and a mathematical transformation of the antenna geometry. After this correction, imaging of active sources is performed using coherent summation of the elastic field over the natural frequencies of the plates, leading to an unique localization of the sources. Imaging mechanical changes in the two plates, instead, is addressed using incoherent summation over the modes, leading to symmetry problems for the plates. This work experimentally illustrates the spatial resolution, perspectives and limitations in the use of eigenmodes to produce images in complex elastic systems of arbitrary shape and materials.

* martin.lott@polito.it

I. INTRODUCTION

Imaging using mechanical waves is a widely used tool not restricted to technological problems. It can be found for example in nature with spiders or bats, which use ultrasounds or elastic waves to scan and image their environment [1, 2]. To be more specific, wave imaging relies on the ability to discern any point in space by recording and processing vibration data. In fluids, if the bulk density ρ and sound celerity c are known, wave diffraction theory can predict in any point and at any time the acoustic wave field inside the medium from measurements at the boundaries [3]. This theory has led to the development of advanced array imaging techniques, used in different fields of research, from wave physics applications [4–7] and medical imaging [8, 9] to seismology [10–12].

In general, a large set of experimental data must be taken into account for the construction of an image. Using matrices to represent and analyze spatiotemporal acoustic data has the advantage of simplifying complex operations like space filtering, beam-forming and wave polarization analysis [13, 14]. In addition, this type of formalism bridges the gap between an analytical formulation and experimental data manipulation, especially with the use of synchronized source/sensor arrays, where the backpropagation operators in space and time can be treated as simple matrix multiplications [3, 15–17]. Usually, diffraction theory for imaging is adopted when the elastic wavelengths are much smaller than the domain to image. In addition, with the use of multi-element arrays, the received waves can be separated based on their arrival direction. This means that the far-field plane waves arriving at the detectors are orthogonal from the receiver array point of view. This limit helps to remove potential unwanted wave reflections and conversions from boundaries, which strongly affect the quality of an image [5].

In the low frequency limit, when the wavelengths are of the same order of magnitude as the domain to be probed, the waves do not propagate and form a so-called standing wave, with discrete resonance effects over frequency. Imaging a medium using its resonant modes is also a wide field of research in itself. Modal Analysis (MA) techniques (also known as System Identification) are used in civil [18], mechanical [19] and aerospace [20] engineering. They are deployed on systems and structures that present complex geometries and boundary conditions, i.e. situations where classical diffraction theory cannot be simply applied [21].

One of the main advantages of MA is that the resonant modes are extended in space.

This means that the entire structure is affected by the vibration, with node and antinode locations that are frequency dependent. Moreover, from an energetic point of view, the lowest frequency modes of a structure gather most of the mechanical energy that the system receives. This restriction in the propagation of energy as a function of frequency for eigenmode may be used to determine the presence of potential defects in a structure, which are very sensitive to the level of vibrational energy[22–27]. However, previous research has shown that among the observable available with MA, the curvature of modal shapes (i.e., the spatial derivative of the modal displacement), and not the resonance frequencies, is the most effective tool for imaging[25, 26, 28], even for a simple one-dimensional structure[21, 26]. This is a strong limitation for the use of modal methods, which consequently require significant instrumentation and mainly surface imaging capabilities.

In the present paper, we propose an experimental realization of modal elastic imaging in an arbitrary elastic system, which draws on both MA and wave diffraction paradigms. The methodology relies on the simultaneous manipulation of multiple discrete modes (eigenmodes), which are present in a highly reverberating system, to image the presence of an active source inside the medium. Similar to the case of traditional elastic imaging methods, one needs to determine the Green's functions for the system to make quantitative comparisons between a model and experimental data. However, in the low frequency regime, there is in general no analytical solution for the Green's function. This is especially true for thin elastic plates with free boundaries, like the one used in the present work. Here, we overcome this limitation with the use of numerical simulations to obtain the eigenfrequencies and eigenmodes of the finite sample. This well-known procedure has yet to be used in this manner for source imaging in elastic systems. The natural frequencies and modal shapes are determined numerically, from a data-driven procedure only requiring knowledge of the sample geometry, enabling to determine the exact elastic properties for the sample under consideration. Subsequently, the numerically calculated modes are combined using a Green's function modal expansion to obtain a semi-analytical propagation model, which can be used to image the system. In addition, from the experimental realization, we highlight the need to exploit the exact receiver positions on the plate surface in the imaging procedure. This requirement is due to the fact that normal modes for the plate are not orthogonal from the receiver point of view, and this leads to post-processing cross-talk between modes and errors

in the image reconstruction. In this paper, we therefore propose and apply a novel and general mathematical method to address this limitation of non-orthogonality. By appropriately combining vibration data and numerical modeling, two imaging problems are addressed: the imaging of an active source and the imaging of a small defect in a reverberating environment. To assess the role of symmetries in the imaging procedures, the experimental setup includes two different thin aluminum plates of different shapes (rectangular and irregular pentagonal). For the source localization problem, a practical situation is chosen where the time emission of the source is unknown, which creates the need to perform another step of phase-locking in the reverberated (coda) part of the transmitted signal. On the other hand, the mass monitoring problem is based on an incoherent summation *in space* over the eigenmodes, which leads to symmetry issues in the resulting images. These symmetry-related errors are driven by the sample geometry only.

The paper is organized as follows. First, we describe the samples and the procedure for acquiring the vibration data. Second, we describe the construction of the digital counterpart of the sample, and the details of the signal processing algorithm. This step holds on synthetic data for illustration purposes of the core of the imaging problem. Third, the experimental source localization images are presented for both samples and compared to the synthetic data. Finally, results and perspectives for defect-like imaging with monitoring techniques using discrete resonant modes are discussed.

II. MATERIALS AND METHODS

A. Experimental set-up

The first sample used in this study is a thin aluminum plate of 3 mm thickness with irregular and non-parallel edges (Fig 1). The particular shape given to the plate guarantees the absence of degenerate modes (i.e. modes with the same resonance frequency but with different modal shapes). Since this study aims to exploit modal imaging concepts, we consider the response at the lowest frequency of the plate. In this frequency regime, the only admitted mode within the plate is the out-of-plane, antisymmetric, dispersive A_0 Lamb mode. For a 3 mm plate, we can determine the wave velocity of this mode from the formula:

$$C_p = \sqrt[4]{\omega^2 \frac{D_0}{h\rho}}; \quad (1)$$

where $D_0 = h^3 E/(12(1-\nu^2))$ is the flexural rigidity, and E, ν, ρ and h are the Young's modulus, Poisson's ratio, bulk density and thickness, respectively. The wavelength is of the order of $\lambda = 50$ cm at 100 Hz, which roughly corresponds to typical plate lateral dimensions (see fig. 1-a), meaning that the 10 lowest modes of this plate should be located around 100 Hz.

The experiment consist in recording at different random locations on the sample the temporal evolution of the wave field generated by various independent active sources. The main purpose of this first experiment is to image the source location, from the analysis of the highly reverberated time signal at the receiver locations. The plate is thus instrumented with 3 piezoelectric disks (ABT-441-RC9, 4.2 kHz central frequency) with a diameter of 27 mm and a thickness of 0.5 mm, which act as the sources. The piezoelectric disks are independently driven with a 2 second chirp signal, with a frequency content ranging from 20 Hz to 900 Hz. This signal is generated by an arbitrary signal generator (Agilent 33500 B), and amplified with an high impedance output tension amplifier (FLC Electonics A400). After propagating in the plate, the vibration response is measured using a Doppler laser vibrometer (Polytech OFV-500 decoder and OFV-505 sensor-head) at 16 different plate locations. The recorded signal is then cross-correlated with the source signal, to provide a 0.5 s highly reverberated impulse response. For each source, the obtained data-set can be represented by a matrix $\mathbf{K_r}(\mathbf{t})$, indexing time at sampling rate intervals and space $r = 1, 2, ..16$ from receiver locations in two dimensions. A schematic of the experiment is shown in Fig. 1-a. Two sources are located on the edges of the plate and one in the center. The receivers are randomly distributed over the plate. A typical example of the 16 recorded signals and their corresponding frequency spectra for a single source are shown in Fig. 1 b-c.

From Fig. 1 panel b-1, one can see that as soon as the signal is emitted, reflected waves appear that mask any potential coherent propagation. From (fig. 1 panel c), the Fourier transforms highlight separated peaks, corresponding to the first resonant modes of the plate.

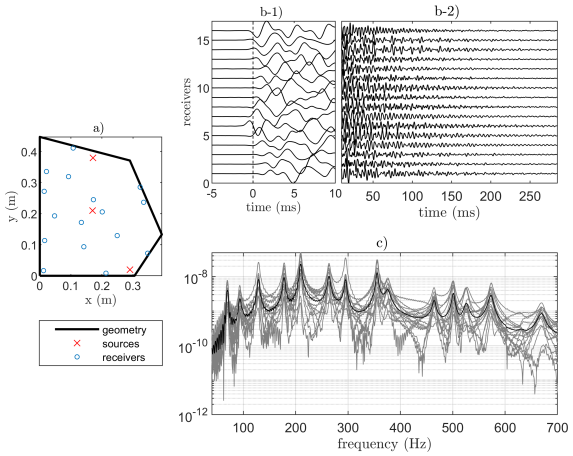

FIG. 1. Irregular plate geometry with its instrumentation. a) For each of the three sources, 16 signals are recorded at the blue location points with a Doppler laser vibrometer, b) with a 300 ms of a strongly reverberated signal (coda). c) In the frequency domain, the signals show clear and isolated resonance peaks. The average of the spectra over the 16 measurement points is represented by the black line.

B. Modal shape determination

The proposed approach exploits knowledge of the modes of vibration to construct a semi-analytical propagating model for the studied sample. There is in the literature a large set of methods able to compute normal modes and associated frequencies for systems with simple geometries [12, 29–31]. Usually, these methods are based on Hamilton's principle of least action, according to which a dynamic system tends to minimize its internal mechanical energy. This minimization principle leads to an eigenvalue problem, with the resonance frequencies as eigenvalues and the normal vibration mode shapes as eigenvector solution of the problem [30]. For the considered plate geometry with Neumann boundary conditions (free edges), analytical models run the risk of non-exhaustively predicting the eigenmodes [19]. A possible solution is to use finite element modeling (FEM) and eigenvalue analysis to obtain the eigenmodes and corresponding eigenfrequencies. The input mechanical parameters (Young's modulus and Poisson's ratio) can then be adjusted to find the best match between the measured and numerically predicted resonance frequencies. This procedure is also know under the name of Resonant Ultrasound Spectroscopy (RUS)[30, 32, 33].

For the source localization procedure to be successful, the numerically calculated and

experimentally derived normal modes should coincide. A way to guarantee this similarity is to perform a systematic spatial projection of numerical modes on the measured ones. This can additionally improve the RUS methodology by simultaneously optimizing the agreement between experimental and numerical data for both the resonant frequencies and modal shapes. To do this, we consider the array response matrix of the three sources s in the frequency domain $\tilde{\mathbf{K}}^{(\mathbf{s})}(\omega)$, projected over the receivers array on the modal shape ϕ_{rn} :

$$B_n(\omega) = \Sigma_s \left| \Sigma_r \tilde{K}_r^{(s)}(\omega)\phi_{rn} \right| \tag{2}$$

$\tilde{\mathbf{K}}^{(\mathbf{s})}(\omega)$ is a matrix, indexed by the *frequencies* and the *receiver index*. This is a table which gathers the measured frequency $\times$ space signals. The product $\tilde{K}_r^{(s)}(\omega)\phi_{rn}$ is therefore a matrix indexed by (*frequency* $\times$ *mode number*).

The starting guess for the mechanical parameter values are $E = 69\ GPa$ for the Young's modulus, $\nu = 0.33$ for the Poisson ration, and $\rho = 2700\ kg.m^{-3}$ for the density , which are the typical aluminum elastic properties. Then, for different Young's modulus and Poisson's ratio values around the starting point, we compute the eigenfrequencies and eigenmodes of the system, and consider the minimization function :

$$g = \Sigma_n \left| \omega_n^d - \omega_n \right| / \omega_n \tag{3}$$

with ω_n^d the angular frequency with the maximum amplitude response of the array projected on the eigenmode ϕ_{rn}, and ω_n the numerical eigenfrequency of this same mode computed from FEM. In this manner, we include the spatial response of the modes in the inversion procedure. Once the minima of g in Eq.3 are found, the results of the projection defined in Eq.2 are depicted in Fig. 2 for optimized mechanical parameters. This figure illustrates the post-processing mode separation over space, with the projection of the experimental data on the numerical eigenmodes. With 16 receivers, the first 13 modes present a maximal projection value $B_n(f = \omega/2\pi)$ at the corresponding eigenfrequency $f_n = \omega_n/2\pi$. Final values are $E = 69.6\ GPa$ for the Young's modulus and $\nu = 0.345$ for the Poisson ratio. Note that an error in the determination of the geometry of the sample could be translated in an uncertainty in the estimated mechanical parameters.

The normalized vibration profiles of the first 16 eigenmodes are shown in Fig 3. The sharp corners used for the design of the plate create a clear separation between modes. From the

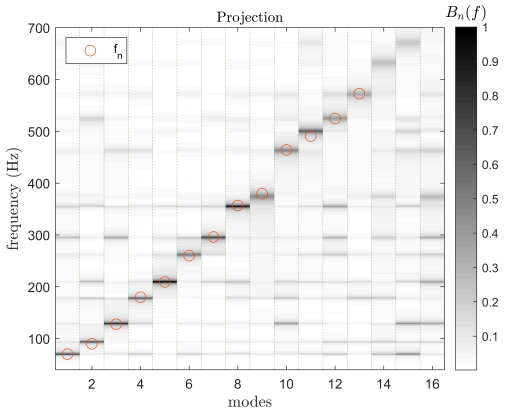

FIG. 2. Frequency response of the normalized modal projection. The red circle represents the eigenfrequency values computed with FEM. The gray-scale represents the continuous response over frequency for each mode, projected (eq.2) on the FEM eigenmodes.

modal fields, the maximum displacement zones appear to be located at the edges of the plate, whilst the nodes of vibrations are principally located in the center of the sample.

C. Modal Green's function expansion and source localization principle

The spatiotemporal evolution of the wave field inside the plate is derived using a universal Green's function expansion method, which only requires knowledge of the normal modal shapes and the associated eigenfrequencies. We start from the expression of the Green's function in the time domain (for $t > 0$)[34–37]:

$$G_{ij}(t) = \Sigma_n \phi_{in} \phi^{\dagger}_{nj} \cos(\omega_n t) \tag{4}$$

where i, j denote the location of two points in the continuous sample domain Ω, n designates the modal index, ω_n the angular eigenfrequency and ϕ_{in} the n-th eigenmode amplitude at the point i. The symbol $.^{\dagger}$ designates the transpose conjugate, and ϕ_{in} are the standing modes, thus represented by real functions. However, Eq.4 is valid for complex function shape too, as soon as they satisfy the wave equation. The time Fourier transform of the Green's function, computed from $t = 0$ to infinity can be expressed as follows :

$$\tilde{G_{ij}}(\omega) = \Sigma_n \phi_{in} \phi^{\dagger}_{nj} \times \delta(\omega - \omega_n) \tag{5}$$

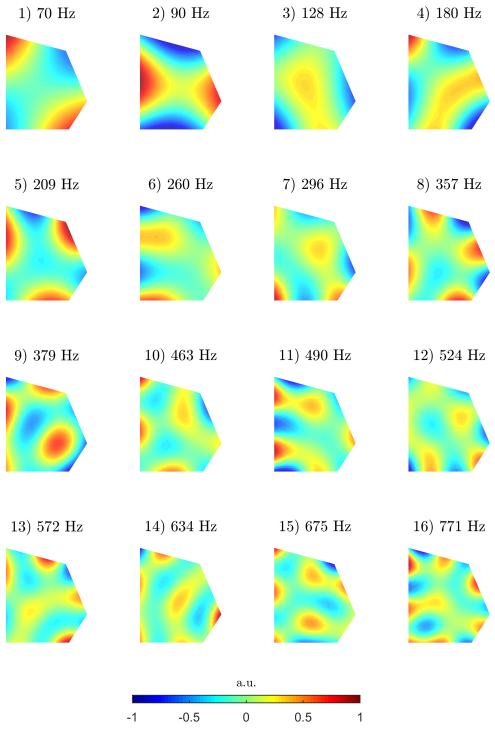

FIG. 3. The 16 first modal shapes of the aluminum plate obtained with FEM.

where $\delta(\omega - \omega_n)$ is the continuous delta function. From this expression, we can express the broadband Green's function, with a continuous integration over frequency:

$$G_{ij} = \int_0^\infty \tilde{G_{ij}}(\omega)\mathrm{d}\omega = \phi_{in}\phi_{nj}^\dagger \tag{6}$$

where we have used Einstein's convention for summation over repeated indices. The upper limit of the continuous sum is determined by the number of modes considered in the imaging problem. With current notations, one should verify:

$$\begin{aligned} \phi_{in}\phi_{nj}^\dagger &= \delta_{ij} \\ \phi_{ni}^\dagger\phi_{in'} &= \delta_{nn'} \end{aligned} \tag{7}$$

where δ_{ij} is the discrete delta function. The first equation indicates that the finite sample response to a source is unique and only depends on its geometrical location. The second equation illustrates the spatial orthogonality of the modal shape functions. To separate the experimental data from theoretical data, the quantity G_{ir} denotes the data set $\mathbf{K_r}(\omega)$, which

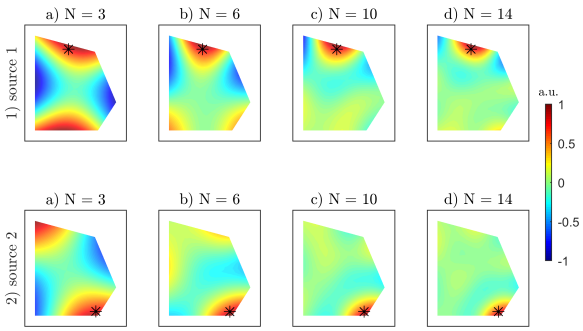

FIG. 4. Synthetic source reconstruction for two different location (1-2) and using 3, 6, 10 and 14 modes respectively.

is the Green's function over frequency, between a source located in an unknown position "i", and a set of receivers located in "r". Because for an arbitrary set of receiving points "r", equations 7 are not satisfied, we present in the following a general method to integrate the geometry of the receiver array. The imaging process then translates the receiving matrix $\mathbf{K_r}(\omega)$ to a single, and frequency accumulated image of the source on the plate surface.

Using these concepts, and the modal responses shown in Fig. 3, we first evaluate the effect of the number of modes on the source reconstruction. From equation 6, the source image is obtained by multiplying the modal amplitude vector at the source location ϕ_{in}, with the modal response matrix at any point location of the sample (and not only the "r" receivers' points) $\phi^{\dagger}_{nj}$. Results are shown in Fig. 4. As expected, increasing the number of modes increases the resolution of the source reconstruction. In addition, the location of the sources also affects the sharpness of the focus.

The central problem of imaging the source lies in the fact that from an experimental point of view, equation 7 is not satisfied when using a small subset of measurement points in the continuous Ω domain. However, it is still possible to construct an image of the source using the composition of Green's function within a set of virtual sources and receiver points r:

$$
\begin{aligned}
G_{ij} &= G_{ir} G_{rj} \\
&= \phi_{in} \phi^{\dagger}_{nr} \phi_{rn'} \phi^{\dagger}_{n'j} \\
&= \phi_{in} V_{nn'} \phi^{\dagger}_{n'j}
\end{aligned} \tag{8}
$$

The matrix $\mathbf{V}$ quantifies the ability of any subsequent set of points r inside the Ω domain to independently identify each mode. If the implicit summation over r is performed on the full domain Ω, the Green's function composition is indeed equivalent to equation 6, and we must verify that:

$$
V_{nn'} = \delta_{nn'} \tag{9}
$$

The projection error due to the limited number of receivers can be corrected. Indeed, with a finite number of modes and receivers, we can determine a new ψ_m basis, constructed as linear combination of the modal shapes ϕ_n. This new basis must be orthonormal from the point of view of the receivers. The construction operation corresponds to the qr-decomposition, which establishes that any rectangular matrix can be decomposed into the product of an orthogonal matrix $\mathbf{Q}$ and an upper triangular matrix $\mathbf{R}$:

$$
\phi^{\dagger}_{nr} = Q_{nm} R_{mr} \tag{10}
$$

where $\mathbf{R}$ matches the receivers to the new basis $\{\psi_m\}$, constructed as linear combination of the modal basis $\{\phi_n\}$. $\mathbf{Q}$ matches the new basis $\{\psi_m\}$ to the modal basis $\{\phi_n\}$. If $\mathbf{R}$ is invertible, the qr-decomposition is unique.

The expression of the Green's function G_{ir} in the new frame basis is noted $G'_{i\{\psi_m\}}$ and can be expressed as:

$$
G'_{i\{\psi_m\}} = G_{ir} R^{-1}_{rm} \tag{11}
$$

Using the correspondence between the $\{\phi_n\}$ and $\{\psi_m\}$ basis, and back-projecting the wave field into each pixel of the image, we can write a potential Green function $\tilde{G_{ij}}$ as:

$$
\tilde{G_{ij}} = G_{ir} R^{-1}_{rm} Q^{\dagger}_{mn'} \phi_{n'j} \tag{12}
$$

We can prove that this expression is the Green's function reconstruction, from the source i to each pixel j, using only r points in the domain Ω. It is valid if the inverse of the matrix $\mathbf{R}$ exists. This means that $\mathbf{R}$ needs to be (but this is not a sufficient condition) a square matrix (i.e. same number of receivers and modes) :

$$\tilde{G_{ij}} = G_{ir} R^{-1}_{rm} Q^{\dagger}_{mn'} \phi^{\dagger}_{n'j} = \phi_{in} \phi^{\dagger}_{nj} = G_{ij} \tag{13}$$

Thus, the imaging principle relies here on the inversion of the matrix $\mathbf{R}$. G_{ir} is a measured quantity, meaning the signal originating from a source and recorded at the receiver locations r, and $\mathbf{Q}$ and $\boldsymbol{\phi}$ are obtained from the QR-decomposition and the FEM model. It is possible to validate the approach with synthetic signals. Here, we limit the example to a single source location, detected with 14 receivers, randomly located over the sample, as shown on fig. 5-a. We first compute the direct, non-corrected, Green's function composition that we applied to the 14 laser measurement point array, following eq. 8. Results are shown in fig.5 b-1 for the matrix $V_{nn'}$ and b-2 for the reconstructed field. The presence of non-zero values on the off-diagonal elements of the $V_{nn'}$ matrix in fig.5 b-1 quantifies the cross-talk between the normal modes due to the limited number of receivers. This leads to spatial errors in the source imaging process. On the other hand, if we apply the qr-decomposition and backproject it using the modified basis (Eq. 12), cross-talk between modes is eliminated and source reconstruction is considerably improved (Fig. 5 c-1 and c-2). Here, signal reconstruction is performed using only a number of receivers equal to the number of modes ($N = 14$).

III. RESULTS

A. Phase locking

Application of the proposed method to real data requires incorporating the effect of time into the modeling. This step is necessary to make a quantitative transition from the measured matrix $\mathbf{K_r}(t)$ and the broadband source model G_{ij}. At time $t = 0$, when the initial pulse is transmitted by the piezoelectric disks, each frequency making up the signal, as a starting point, acquires the phase of the modal shapes at the source location. For stationary modes, this original phase is equal to 0 or π. If this phase information is lost, i.e. we no longer know when the pulse was emitted, the resulting sum in equation 6 leads to an

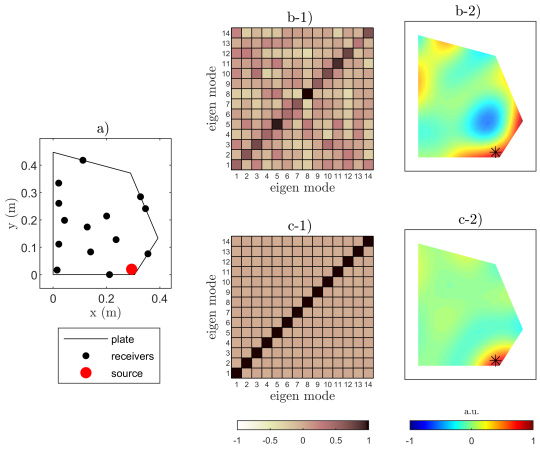

FIG. 5. Principle of source reconstruction with synthetic data. a) Specimen geometry with virtual receivers and source location. b) Using direct Green's function composition leads to a distortion of the matrix $V_{nn'}$ (Eq. 9) (b-1) and errors in the reconstructed signal (b-2). c) Using the array correction, each virtual mode is independent (c-1) and returns an exact image of the source, for the considered modes combination (c-2).

incoherent summation of the modes and to the loss of spatial resolution. A general method for the inversion of the time origin of an active source is presented in [16]. We propose here a simpler solution to this problem, exploiting the fact that the space-time Fourier transform of the receiver array is real, according to Eq. 5.

$\mathbf{K_r(t)}$ is the matrix of receiver data, which records the temporal coda (reverb) signal from a single source in the plate, transmitted at time $t = 0s$ but recorded starting at an unknown time $t_0 > 0s$. For each resonant mode, we consider the delayed-time Fourier transform of the spatial projection, computed from time $t = t_0$ over a time window T:

$$\tilde{F}_n(\omega, t_0 - \tau) = \exp\left(i\omega(t_0 - \tau)\right) \int_0^T K_r(t)\phi_{rn} \exp\left(i\omega t\right) \mathrm{dt} \tag{14}$$

Since $\tilde{F}_n(\omega, t_0 - \tau)$ should be real for all n, we look for the minimum of the function:

$$h_{t_0}(\tau) = \frac{1}{N}\Sigma_n \frac{\left|\Im\left\{\tilde{F}_n(\omega_n, t_0 - \tau)\right\}\right|}{\left|\tilde{F}_n(\omega_n, t_0 - \tau)\right|} \tag{15}$$

where $\Im$ indicates the imaginary part operator. This procedure is graphically illustrated in Fig. 6. In panel a), the signal emitted from source 2 to receiver 5 is shown. From this signal, we apply a Hanning time window in the late part of the coda, starting at $t_0 = 20$ ms, shown in panel b). For eight of the modes with the best signal to noise ratio, the function $\tilde{F}_n(\omega, t_0 - \tau)$ is computed and depicted in panel c). For $\tau = 20$ ms, all modes are synchronized, which corresponds to the delay $\tau = t_0$. The sum over the modes $h_{t_0}(\tau)$ is presented in sub panel c). Thus, even if t_0 (i.e. the temporal origin of the signal) is unknown, it is possible to trace back the origin of the signal using the spatiotemporal analysis of the coda. This is used as a "phase locking" method on the data through the $\tilde{F}_n$ function. Once τ is found, the Green function is estimated as the coherent sum of the delayed Fourier transform of the receiver matrix $\mathbf{K}_r(t)$:

$$G_{ir} = \int_0^\infty \tilde{\mathbf{K}}_r(\omega) \exp\left(-i\omega\tau\right) \mathrm{d}\omega \tag{16}$$

With i the source location (unknown) and r the receiver locations. Rather than using short and impulsive source signals, we use here the stability of the Fourier transform computed over a large window to measure each of the modal amplitudes. This measurement stability may be disrupted when noise becomes prominent in the reverberated signal. From our experimental data, we can analyze the first 200 ms of reverberated signal only, before the measurement is dominated by uncorrelated noise.

B. Experimental source localization

In order to experimentally determine the source location in the considered plate, the real part of the Fourier transform after the phase correction is summed over the eigenfrequencies according to Eq.6 and the resulting vector is back-propagated according to Eq. 12. The theoretical reconstruction model for three examples of source location on the considered plate is displayed Fig. 7-a, experimental results are shown in Fig. 7-b, and the reconstruction without correction in Fig. 7-c. The images in Fig. 7-b show that the reconstruction is effective in determining the location close to the expected theoretical image (Fig.7-a), although the resolution is in some cases limited. In Fig.7, we only use a reduced number of modes with the highest signal to noise ratio in the reconstruction and adapt the array size to keep the possibility to compute the inverse matrix $\mathbf{R}^{-1}$ in equation 12. The reduction of

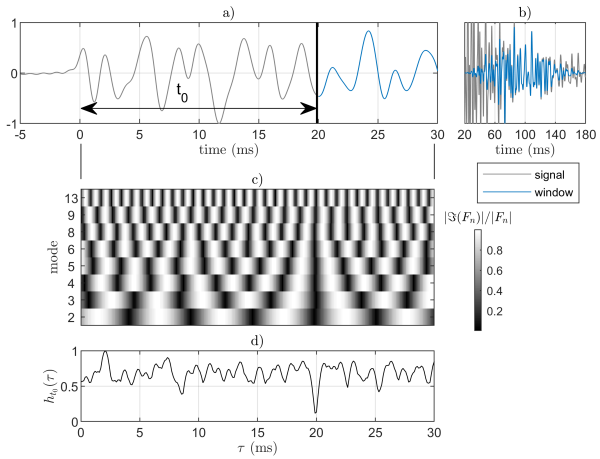

FIG. 6. Phase locking method. a) Time signal emitted from source 2 and recorded at location 5. The considered time window for the analysis starts at time $t_0 = 20\ ms$, highlighted with the black vertical line. b) Hanning time window considered for the analysis (blue signal) of length $T = 160\ ms$ in the late coda part of the total transmitted signal (gray signal). c) Imaginary part contribution of the Fourier transform for 8 modes with the highest signal to noise ratio. d) At $\tau = t_0 = 20\ ms$, all the modes are in sync, which corresponds to a minimum for the function $h_{t_0}(\tau)$

the number of useful modes is due to the imperfection of the source, which does not provide a perfectly flat response in the considered frequency range. In addition, if the source is located on a vibration node of the plate, this mode cannot be excited. These are limiting factors in the efficiency of the method. In the present work, we use the modal amplitude directly estimated in the late coda part of the signal, without further post-processing and we only consider modes with the highest signal to noise ratio. A more accurate approach would need to invert location and modal normalization at the same time.

C. Application to regular geometry

To evaluate the influence of specimen geometry, we produce the same data-set as previously on a 3 mm thick rectangular aluminum plate. Both plates have the same thickness and approximately the same lateral dimensions. For the determination of the modal shapes, we adopt here a semi-analytical method, the xyz algorithm [30]. The resulting first 16 eigenmodes and eigenfrequencies calculated using this method are shown in Fig. 8.

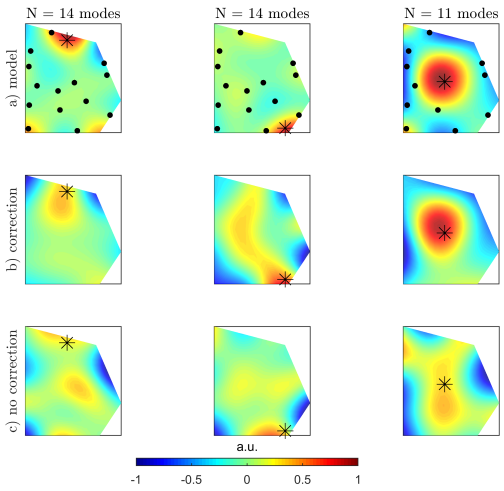

FIG. 7. Images of the reconstruction. panels a) show the expected image with the used receivers as black points and the source as a black star. b) the main resulting image after corrections. Panels c) show the results without correction, for comparison purpose. The images are normalized by the maximum of their absolute value.

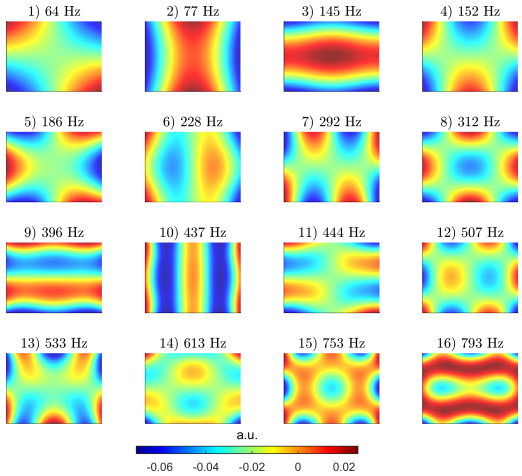

FIG. 8. The 16 first modal shape of the rectangular aluminum plate

Fig. 9 illustrates graphically the results of source localization in three examples for this plate geometry. There is good agreement between the model and the data. In this experiment, only 9 modes are correctly detected and therefore used in the source reconstruction. The number of points used is also reduced to 9, in order to use equation 12.

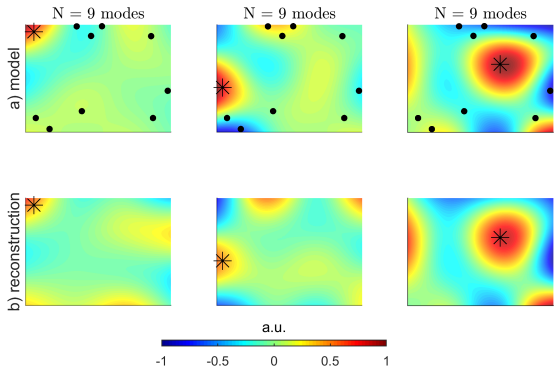

FIG. 9. Sources localization results in the rectangular plate. a) expected image, built from direct Green's function modal expansion. The black dots represents the used receivers for the imaging, and the title specify the number of modes used for the reconstruction. b) reconstruction with the data. The images are normalized by the maximum of their absolute value.

IV. DEFECT LOCALIZATION

The second experiment presented in this work illustrates the feasibility of using the modal imaging method for the detection of inhomogeneities in the tested samples. This is realized by placing a small point mass on the surface of the plates and acquiring the same data set as previously (3 sources, 16 receiver points). The test is performed with both the rectangular and the irregularly shaped plates. Experimentally, a simple perturbation of the dynamic response of the plate is obtained by adding a small mass at its surface. The added mass consists of small cubic permanent magnets. The estimated added mass is around 5g for both plates, which is large enough to be detected but small enough not to change the system overall response. It is possible to use perturbation theories to model this small change in the structure [20, 38]. As a first approximation, we assume here that a change of mass does not affect the eigenmodes shapes $\{\phi_n\}$ but only the eigenfrequencies f_n [27]. This assumption leads to considerable simplifications by neglecting the details of the mechanical interaction of the mass with the plate. Consequently, the mass location can be deduced from the sensitivity of the modes to its addition [39].

We first compare the data set obtained on the pentagonal plate with and without the added mass. The signature of the added mass on the signals is shown in Fig. 10. From the frequency analysis of the data (Fig.10 a-b), the addition of mass induces a shift of the

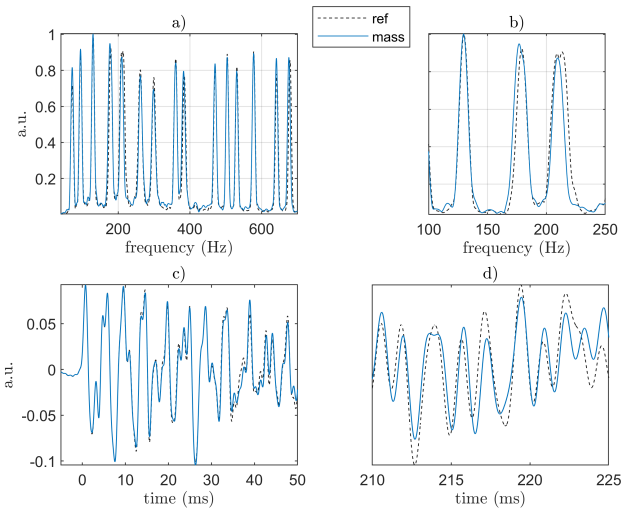

FIG. 10. Signal signatures due to the addition of localized mass. a) The amplitudes and the resonant frequencies are affected by the add of mass. b) (zoom in panel a) The mass decreases the initial resonant frequencies. c) In the time domain, the shift of the resonances are translated into a cumulative phase shift in the coda signal. d) same as c) with a zoom in the 30-60 ms time window.

resonant curves to lower frequencies and a modulation of the peak amplitudes. In the time domain (Fig.10 c-d), we observe the typical cumulative time shift of the coda [40], induced here by the changes of the resonant frequencies. From this complex signature, we choose to retain only the frequency shift of the modes as the main localization parameter and propose the following simplified imaging function :

$$I_i = \Sigma_n \frac{\delta f_n}{f_n} \left|\phi^{\dagger}_{ni}\right| \tag{17}$$

Where i indicates the pixel of the image to be constructed, f_n the n^{th} resonance frequency for the unperturbed plate, and δf_n the variation of a resonance frequency between the reference and perturbed states.

Results of this imaging procedure are shown in Fig. 11 for both rectangular (a) and irregular (b) plates. Since perturbation theory is applied on a mode at a time, it is not possible to perform coherent summations over frequencies as in the previous source localization problem. Thus, localizing a change in a structure from the analysis of individual resonances results in symmetry problems during the data post-processing. For a rectangular shaped structure, the incoherent summation over the modes of the wavefield shown in

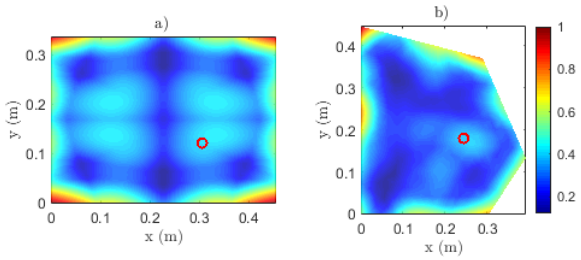

FIG. 11. Mass localization results for a) the rectangular plate with an add mass of 7.2g and b) for the pentagonal plate with an add of mass of 3.6g. the mass is a small magnet depicted with the red circle in panels a-b. The images are normalized by the maximum of their absolute value.

equation 17 leads to four symmetric source images. The irregular pentagonal plate, instead, demonstrates greater uniqueness in the potential location of the mass.

In Fig. 11, the edges of the plates show the largest incoherent cumulative amplitudes of vibration. The use of sharp corners for the two plates helps to split the different resonant modes across frequencies, but also induces nonuniform localization of the vibration energy for the resonant modes. Plates with smooth edges provides a more uniform spatial spread of the energy, and thus modal overlapping over frequency [41, 42], which may add complexity to the modal decomposition technique. The resulting image, built from equation 17, does not take into account the spatial inhomogeneity of the coherent sum over the modes. This is also a factor preventing access to the mass of the added object, as it should be inverted jointly with its location.

V. CONCLUSIONS

In this paper, we have presented the experimental realization of a source and defect-like elastic imaging procedure, using discrete normal modes of plates with arbitrary geometries. The imaging methodologies are based on data-driven procedures, which couple numerical simulations with experimental data.

The first experiment, i.e. source localization, uses a modal Green's function expansion and composition. Sources are shown to be reliably imaged using a coherent sum over the discrete resonant modes supported by the plates, with a mathematical correction for the

receiver array geometry. With the limited number of modes and receivers used in both plates, the resolution of the images are limited but could be applied to any kind of geometry.

The second imaging problem, i.e. mass localization, is handled with an incoherent summation over the same modes, and can lead to symmetry problems due to the plate geometries in the formation of the final images. The incoherent summation of the modes induces four symmetric mass images in the rectangular cavity, and a single one in the irregular pentagonal cavity. For both cavities, the modal intensity is not homogeneous and creates an over-representation of the plate edges in the images.

If the vibration amplitude is large enough, the interaction of the mass with the plate can generate harmonics in a nonlinear regime. These harmonics can be used for imaging, by treating the defect as an auxiliary source. However, the defect must have an impedance comparable to the plate to be treated as an auxiliary source of nonlinear harmonics in the low frequency regime. Another important aspect it that the plate is an anharmonic cavity, meaning that normal modes are not necessarily multiples of fundamental frequencies. The harmonics due to the presence of a defect can alternatively be evanescent, remaining in the defect area, or strongly amplified, if one of the generated harmonics falls on a fundamental mode of the plate. In future, the coherent source imaging technique could be used in reversed mode, using few sources and adapting an array geometry to focus a high level of energy anywhere inside a medium, even at depth, without the need to physically access the targeted point. We will address this method in future work.

ACKNOWLEDGMENTS

We wish to thank Andrea Colombi for valuable discussions and suggestions. All authors are supported by the European Commission under the FET Open "Boheme" Grant No. 863179.

REFERENCES

[1] F Bosia, V Dal Poggetto, AS Gliozzi, G Greco, M Lott, M Miniaci, F Ongaro, M Onorato, SF Seyyedizadeh, M Tortello, et al. Optimized structures for vibration attenuation and sound control in nature: a review. arXiv preprint arXiv:2201.05795, 2022.

[2] Vinícius F Dal Poggetto, Federico Bosia, Gabriele Greco, and Nicola M Pugno. Prey impact localization enabled by material and structural interaction in spider orb webs. Advanced Theory and Simulations, page 2100282, 2021.

[3] Arthur B Baggeroer, WA Kuperman, and Henrik Schmidt. Matched field processing: Source localization in correlated noise as an optimum parameter estimation problem. The Journal of the Acoustical Society of America, 83(2):571–587, 1988.

[4] Claire Prada, Sébastien Manneville, Dimitri Spoliansky, and Mathias Fink. Decomposition of the time reversal operator: Detection and selective focusing on two scatterers. The Journal of the Acoustical Society of America, 99(4):2067–2076, 1996.

[5] Alexandre Aubry and Arnaud Derode. Detection and imaging in a random medium: A matrix method to overcome multiple scattering and aberration. Journal of Applied Physics, 106(4):044903, 2009.

[6] Alexandre Aubry, Laura A Cobus, Sergey E Skipetrov, Bart A Van Tiggelen, Arnaud Derode, and John H Page. Recurrent scattering and memory effect at the anderson localization transition. Physical review letters, 112(4):043903, 2014.

[7] Eric Larose, Thomas Planes, Vincent Rossetto, and Ludovic Margerin. Locating a small change in a multiple scattering environment. Applied Physics Letters, 96(20):204101, 2010.

[8] Jean-Luc Robert and Mathias Fink. Green's function estimation in speckle using the decomposition of the time reversal operator: Application to aberration correction in medical imaging. The Journal of the Acoustical Society of America, 123(2):866–877, 2008.

[9] Massimiliano Fasi, Nicholas J Higham, and Bruno Iannazzo. An algorithm for the matrix lambert w function. SIAM Journal on Matrix Analysis and Applications, 36(2):669–685, 2015.

[10] Andrea Colombi, Julien Chaput, Florent Brenguier, Gregor Hillers, Philippe Roux, and Michel Campillo. On the temporal stability of the coda of ambient noise correlations. Comptes Rendus Geoscience, 346(11-12):307–316, 2014.

[11] Rita Touma, Thibaud Blondel, Arnaud Derode, Michel Campillo, and Alexandre Aubry. A distortion matrix framework for high-resolution passive seismic 3-d imaging: application to the san jacinto fault zone, california. Geophysical Journal International, 226(2):780–794, 2021.

[12] Piero Poli, Michel Campillo, and Maarten de Hoop. Analysis of intermediate period correlations of coda from deep earthquakes. Earth and Planetary Science Letters, 477:147–155, 2017.

[13] Valerio Poggi and Donat Fäh. Estimating rayleigh wave particle motion from three-component array analysis of ambient vibrations. Geophysical Journal International, 180(1):251–267, 2010.

[14] Léonard Seydoux, Julien de Rosny, and Nikolai M Shapiro. Pre-processing ambient noise cross-correlations with equalizing the covariance matrix eigenspectrum. Geophysical Journal International, 210(3):1432–1449, 2017.

[15] William Lambert, Laura A Cobus, Thomas Frappart, Mathias Fink, and Alexandre Aubry. Distortion matrix approach for ultrasound imaging of random scattering media. Proceedings of the National Academy of Sciences, 117(26):14645–14656, 2020.

[16] Michael D Collins and WA Kuperman. Focalization: Environmental focusing and source localization. The Journal of the Acoustical Society of America, 90(3):1410–1422, 1991.

[17] Mathias Fink, Didier Cassereau, Arnaud Derode, Claire Prada, Philippe Roux, Mickael Tanter, Jean-Louis Thomas, and François Wu. Time-reversed acoustics. Reports on progress in Physics, 63(12):1933, 2000.

[18] Ariana Lucia Astorga, Philippe Gueguen, Jacques Riviere, Toshihide Kashima, and Paul Allan Johnson. Recovery of the resonance frequency of buildings following strong seismic deformation as a proxy for structural health. Structural Health Monitoring, 18(5-6):1966–1981, 2019.

[19] Ivo Senjanović, Marko Tomić, Nikola Vladimir, and Neven Hadžić. An analytical solution to free rectangular plate natural vibrations by beam modes–ordinary and missing plate modes. Transactions of FAMENA, 40(3):1–18, 2016.

[20] A Agneni, L Balis Crema, A Castellani, and F Mastroddi. Damage detection on aeronautical structures by a mixed approach in the frequency domain. volume 2768, page 1415, 1996.

[21] Philippe Roux, Philippe Guéguen, Laurent Baillet, and Alaa Hamze. Structural-change localization and monitoring through a perturbation-based inverse problem. The Journal of the Acoustical Society of America, 136(5):2586–2597, 2014.

[22] Peter Cawley and Robert Darius Adams. The location of defects in structures from measurements of natural frequencies. The Journal of Strain Analysis for Engineering Design, 14(2):49–57, 1979.

[23] Charles R Farrar and David A Jauregui. Comparative study of damage identification algorithms applied to a bridge: I. experiment. Smart materials and structures, 7(5):704, 1998.

[24] Jag Humar, Ashutosh Bagchi, and Hongpo Xu. Performance of vibration-based techniques for the identification of structural damage. Structural Health Monitoring, 5(3):215–241, 2006.

[25] Jesús N Eiras, Cédric Payan, Sandrine Rakotonarivo, and Vincent Garnier. Damage detection and localization from linear and nonlinear global vibration features in concrete slabs subjected to localized thermal damage. Structural Health Monitoring, 20(2):567–579, 2021.

[26] Koen Van Den Abeele. Multi-mode nonlinear resonance ultrasound spectroscopy for defect imaging: An analytical approach for the one-dimensional case. The Journal of the Acoustical Society of America, 122(1):73–90, 2007.

[27] Martin Lott, Cedric Payan, Vincent Garnier, Pierre-Yves Le Bas, Timothy James Ulrich, and Marcel C Remillieux. Three-dimensional modeling and numerical predictions of multimodal nonlinear behavior in damaged concrete blocks. The Journal of the Acoustical Society of America, 144(3):1154–1159, 2018.

[28] AS Gliozzi, M Nobili, and M Scalerandi. Modelling localized nonlinear damage and analysis of its influence on resonance frequencies. Journal of Physics D: Applied Physics, 39(17):3895, 2006.

[29] Yongliang Wang, Xinwei Wang, and Yong Zhou. Static and free vibration analyses of rectangular plates by the new version of the differential quadrature element method. International Journal for Numerical Methods in Engineering, 59(9):1207–1226, 2004.

[30] A_ Migliori, JL Sarrao, William M Visscher, TM Bell, Ming Lei, Z Fisk, and R Gi Leisure. Resonant ultrasound spectroscopic techniques for measurement of the elastic moduli of solids. Physica B: Condensed Matter, 183(1-2):1–24, 1993.

[31] T Mizusawa. Natural frequencies of rectangular plates with free edges. Journal of Sound and Vibration, 105(3):451–459, 1986.

[32] Brian J Zadler, Jérôme HL Le Rousseau, John A Scales, and Martin L Smith. Resonant ultrasound spectroscopy: theory and application. Geophysical Journal International, 156(1):154–169, 2004.

[33] Marcel C Remillieux, TJ Ulrich, Cédric Payan, Jacques Rivière, Colton R Lake, and Pierre-Yves Le Bas. Resonant ultrasound spectroscopy for materials with high damping and samples of arbitrary geometry. Journal of Geophysical Research: Solid Earth, 120(7):4898–4916, 2015.

[34] Richard L Weaver and John Burkhardt. Weak anderson localization and enhanced backscatter in reverberation rooms and quantum dots. The Journal of the Acoustical Society of America, 96(5):3186–3190, 1994.

[35] Thomas Gallot, Stefan Catheline, and Philippe Roux. Coherent backscattering enhancement in cavities. highlights of the role of symmetry. The Journal of the Acoustical Society of America, 129(4):1963–1971, 2011.

[36] Stefan Catheline, Thomas Gallot, Philippe Roux, Guillemette Ribay, and Julien De Rosny. Coherent backscattering enhancement in cavities: The simple-shape cavity revisited. Wave motion, 48(3):214–222, 2011.

[37] Philippe Guéguen, Pierre-Yves Bard, and Francisco J Chávez-García. Site-city seismic interaction in mexico city–like environments: An analytical study. Bulletin of the seismological society of America, 92(2):794–811, 2002.

[38] LY Yam, TP Leung, DB Li, and KZ Xue. Theoretical and experimental study of modal strain analysis. Journal of Sound and vibration, 191(2):251–260, 1996.

[39] Zhi-Fang Fu and Jimin He. Elsevier, 2001.

[40] Roel Snieder, Alexandre Grêt, Huub Douma, and John Scales. Coda wave interferometry for estimating nonlinear behavior in seismic velocity. Science, 295(5563):2253–2255, 2002.

[41] Andrea Colombi, Lapo Boschi, Philippe Roux, and Michel Campillo. Green's function retrieval through cross-correlations in a two-dimensional complex reverberating medium. The Journal of the Acoustical Society of America, 135(3):1034–1043, 2014.

[42] Martin Lott, Philippe Roux, Léonard Seydoux, Benoit Tallon, Adrien Pelat, Sergey Skipetrov, and Andrea Colombi. Localized modes on a metasurface through multiwave interactions. Physical Review Materials, 4(6):065203, 2020.

Declaration of Interest Statement

Source and defect localization in thin elastic plates of arbitrary geometry using eigenmodes

Martin Lott, Antonio S. Gliozzi and Federico Bosia

Authors declare they have no competing interest in the submission of this work.

Sincerely,

Martin Lott